A Letters Journal Exploring the Frontiers of Physics

August 2018

EPL, **123** (2018) 44004
doi: 10.1209/0295-5075/123/44004

www.epljournal.org

Enhancing thermal rectification in graphene-carbon nanotube junctions by tuning the chirality of pillar

Xueming Yang[1(a)], Sihan Wu[1], Jiangxin Xu[1], Dapeng Yu[1] and Bingyang Cao[2(b)]

[1] *Department of Power Engineering, North China Electric Power University - Baoding 071003, China*
[2] *Key Laboratory for Thermal Science and Power Engineering of Ministry of Education, Department of Engineering Mechanics, Tsinghua University - Beijing 100084, China*

received 25 June 2018; accepted in final form 27 August 2018
published online 21 September 2018

PACS 44.10.+i – Heat conduction
PACS 65.80.-g – Thermal properties of small particles, nanocrystals, nanotubes, and other related systems
PACS 63.22.-m – Phonons or vibrational states in low-dimensional structures and nanoscale materials

Abstract – This letter investigates thermal rectification (TR) in graphene-carbon nanotube (GN-CNT) junctions formed by SWCNT(12, 12) connected with a single-layer graphene nanosheet (GN-SWCNT(12, 12)). It is found that the TR ratio of GN-SWCNT junction can be enhanced dramatically by tuning the chirality of the pillar. TR ratio of the GN-SWCNT(12, 12) junction can respectively reach up to 1487% and 2586.4% at temperatures of 300 K and 200 K ($|\Delta| = 0.5$), much higher than those previously reported for the pillared graphene and GN-CNT junctions. The influences of the geometric parameters on the thermal rectification are discussed. The results could offer useful guidelines to the design and performance improvement of the GN-CNT–based thermal rectifier.

Introduction. – The pillared graphene system (PGS) [1] has attracted considerable attention due to its broad potential applications such as in new efficient electrodes for batteries and fuel cells [2], advanced thermal management materials [3,4], high-performance supercapacitors [5], and nanoporous structures for hydrogen/gas storage [1]. In real experimental samples, the PGS may consist of graphene layers covalently bonded with nanotubes with different helicities. PGS properties rely on their building blocks, CNT-graphene junctions; thus, understanding the properties of CNT-graphene junctions and the effects of their geometrical structure is crucial for the design and application of PGS-based nanomaterials and nanodevices.

The stability and geometrical structures of CNT-graphene junctions and junction arrays were previously studied by González *et al.* [6,7]. They found that the armchair and $(6n, 0)$ geometries with n equal to a multiple of 3 allowed for the formation of standing waves between the junction and the other end of the tube. Extensive studies [3,8–11] have been carried out to investigate heat conduction in PGS, however, PGSs with pillars using SWCNT(6, 6) were solely considered in most of these studies. Recently, Zhang *et al.* [12] probed the topology and thermal conductance of 3D nanotube-graphene cone junctions in which the diameter of the CNTs was approximately 20 Å. They found that the geometry of the connecting region influenced the conductance of the junction.

As a fundamental device for heat transport control and phononics, the thermal rectifier allows heat/phonon to flow preferentially in one direction. Thermal rectifiers have great potential in thermal management and phononics circuit applications. To obtain a more efficient thermal rectifier, many studies have been conducted to explore new nanostructures with a TR effect and to study novel TR mechanisms [13–22]. It has been reported that the designed graded PGS and a single GN-SWCNT junction with SWCNT(6, 6) as pillar(s) (GN-SWCNT(6, 6) junction) exhibited an ultrahigh thermal rectification (TR) ratio [23,24]. However, how pillars with different chiralities affect the thermal rectification of PGS and CNT-graphene junctions remains unknown. In this paper,

(a) E-mail: xuemingyang@ncepu.edu.cn (corresponding author)
(b) E-mail: caoby@tsinghua.edu.cn (corresponding author)

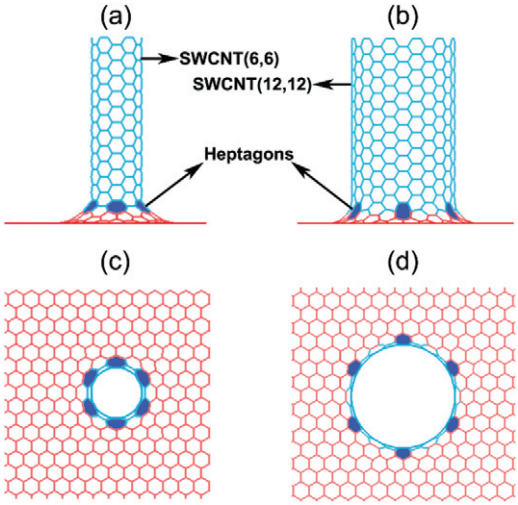

Fig. 1: (Colour online) Comparison of the structures diagram of a GN-SWCNT(12, 12) junction and a GN-SWCNT(6, 6) junction. (a) and (c): front view and aerial view of the GN-SWCNT(6, 6) junction, respectively; (b) and (d): front view and aerial view of the GN-SWCNT(12,12) junction, respectively.

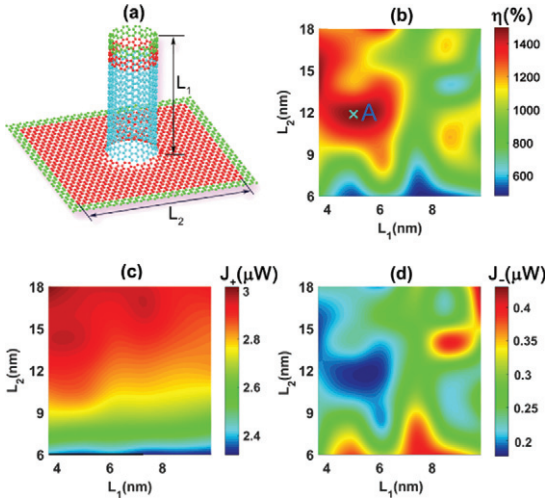

Fig. 2: (Colour online) (a) Schematic diagram of a GN-SWCNT(12, 12) Junction for calculation of thermal rectification; (b), (c) and (d): 2D view of the distribution of the TR ratio η, J_+, J_- with respect to L_1 and L_2 for GN-SWCNT(12, 12) junction, respectively.

classical non-equilibrium molecular-dynamics (NEMD) simulations are used to investigate thermal rectification for GN-SWCNT(12, 12) junctions. Results demonstrate that the TR ratio of GN-CNT junction can be further enhanced by using a pillar with different chirality.

Simulations. – Figure 1 compares the atomic structures of a GN-SWCNT(6, 6) junction and a GN-SWCNT(12, 12) junction. Both of them have six heptagons at the junction, concurring with Euler's rule and the results of Zhang *et al.* [12]. However, the graphene nanosheet and the tube in the connecting region of the GN-SWCNT(6, 6) junctions need to be bent more severely than in the GN-SWCNT(12, 12) junction due to the smaller diameter of SWCNT(6, 6).

In our simulations, classical NEMD method is adopted. NEMD simulations are performed using the LAMMPS software package [25]. In all simulations, the TR system of the GN-CNT junction is divided into three parts: fixed parts, thermostated parts, and free parts. Along the tube's longitudinal direction, the side of the graphene nanosheet(s) is hereafter referred to as the wide side, and the open end of the tube is referred to as the narrow side. The optimized Tersoff potential [26] is adopted to model the C–C interactions for the GN-CNT junction, which could provide conductivity value consistent with the experiment for carbon materials [4,22]. The atoms in the fixed parts at both sides are fixed to obtain a suspended structure, and the free boundary condition is applied in all directions.

The system is first relaxed in the NVT ensemble at 300 K for 5×10^6 time steps (0.4 fs/step) with a Nosé-Hoover thermostat. Then, NEMD is performed for another 12×10^6 steps in the NVE ensemble to establish a temperature gradient along the longitudinal direction of the tube using a Berendsen thermostat [27] to study the nonlinear thermal transport processes [15,28]. Temperatures in the two thermostated regions on the wide and narrow sides are respectively set at $T_0(1+\Delta)$ and $T_0(1-\Delta)$; T_0 represents the average temperature, and Δ represents the normalized temperature difference. The TR ratio is computed as

$$\eta = \frac{(J_+ - J_-)}{J_-} \times 100\%, \tag{1}$$

where J_+ is the heat current from the wide side to the narrow side when $\Delta > 0$, and J_- is the heat current from the narrow side to the wide side when $\Delta < 0$.

The vibration density of states (vDOS) or phonon power spectra has been widely used for the analysis and explanation of TR and heat conduction behaviour in nanostructure systems. The vDOS is calculated by Fourier transform of the velocity autocorrelation functions of the simulated systems. The vDOS of the i-th atom, $D_i(f)$, is defined as

$$D_i(f) = \int \langle v_i(0) \cdot v_i(t) \rangle e^{-2\pi i f t} \mathrm{d}t, \tag{2}$$

where $v_i(t)$ is the velocity vector of the i-th atom at time t and $\langle \cdots \rangle$ indicates an ensemble average.

The schematic diagram for simulations of TR in GN-SWCNT(12, 12) junctions is shown in fig. 2(a), where green, red and cyan areas denote the fixed part, thermostated part and free part of the system. L_1 denotes the height of the tube from its top end to the graphene nanosheet, and L_2 denotes the side length of the square graphene nanosheet (excluding its fixed part) where the width of the fixed region is set to 0.4 nm.

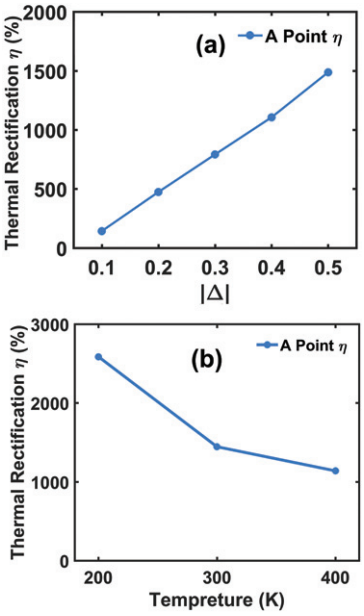

Fig. 3: (Colour online) TR ratio as a function of $|\Delta|$ and average temperature for the GN-SWCNT(12, 12) junction with geometry size sets A.

Results and discussion. – The 2D gridded data of the TR ratio by L_1 varied from 3.69 to 9.84 nm (15–40 unit cells) with a step of five unit cells; L_2 varies from 6 to 18 nm with a step of 2 nm as calculated by MD simulations. T_0 is set at 300 K, and $|\Delta|$ is set at 0.5. Then, a cubic interpolation is followed on the gridded simulation results to obtain a smoother TR ratio distribution with respect to L_1 and L_2; see fig. 2(b). The corresponding J_+ and J_- are shown in fig. 2(c) and (d), respectively. Figure 2(b) shows that GN-SWCNT(12, 12) junctions exhibit an ultrahigh TR ratio within an optimal geometric size. The maximum TR ratio is at A point in fig. 2(b) with a value of 1487%, and the corresponding sizes are $L_1 = 4.9$ nm and $L_2 = 12$ nm.

The TR ratios for the GN-SWCNT(12, 12) junction with geometry size sets A almost increase linearly with an increase of $|\Delta|$ in the range from 0.1 to 0.5 as shown in fig. 3(a). This observation is similar to the previous results [29,30]. In addition, the TR ratios decrease with an increase in average temperature (fig. 3(b)). Such variations are similar to those presented in the previous literature [31,32], which can be explained as the weakening effect of Umklapp scattering. The TR ratio can reach 2586.4% at a temperature of 200 K. The maximum TR ratios are approximately 20% and 53.8% larger than those of the reported GN-SWCNT(6, 6) junction [24] at temperatures of 300 K and 200 K ($|\Delta| = 0.5$), respectively. Therefore, we demonstrate that the TR ratio of GN-SWCNT junction can be further enhanced by choosing a pillar with a different chirality.

To understand the ultrahigh TR ratio exhibited in the GN-SWCNT(12, 12) junctions, we calculate the vDOS and the velocity autocorrelation function (VACF) for the

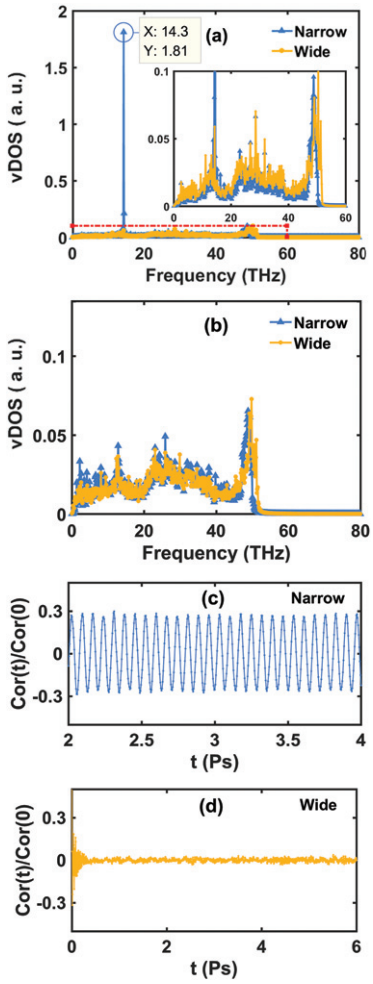

Fig. 4: (Colour online) vDOS per atom and VACF for the GN-SWCNT(12, 12) junction with geometry size sets A. (a) vDOS when $\Delta = -0.5$; (b) vDOS when $\Delta = 0.5$; (c) and (d): VACF for narrow and wide sides when $\Delta = -0.5$.

GN-SWCNT(12, 12) junction with geometric size set A: $L_1 = 4.9$ nm and $L_2 = 12$ nm, as shown in fig. 4. The atoms of the tube in the first two unit cells beside each thermal contact are chosen to calculate vDOS and VACF. The regional vDOS is calculated from the Fourier transform of the VACF. In fig. 4(a), significant sharp peaks at 14.3 THz are observed in the power spectra for the narrow side under $\Delta = -0.5$ but did not appear in the power spectra for the wide side. The significant peak at 14.3 THz is demonstrated to be a standing wave with a frequency of 14.3 THz by VACFs as shown in fig. 4(c). This type of vDOS peak and the standing wave are identified and discussed in detail in previous studies [16,17,23,24], explained by the local resonance that occurred only when $\Delta < 0$ for the narrow end of the graded nanostructure. The frequency of 14.3 THz for the vDOS peak and the standing wave is slightly less than that of 14.5 THz for those in GN-SWCNT(6, 6) junctions reported previously [24]. The physical essence of the vDOS peak is actually the transverse acoustic wave or standing wave as suggested by

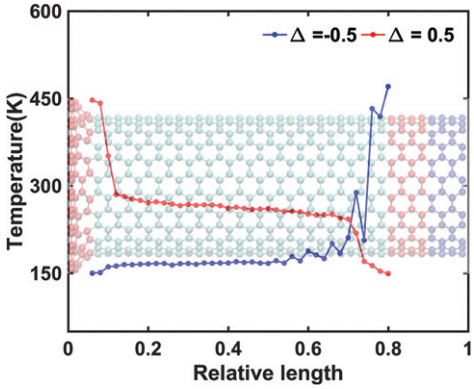

Fig. 5: (Colour online) Temperature profile of GN-SWCNT(12, 12) with geometry size sets A along the heat transport direction.

other studies [16,33]. The vDOS peak in this paper is the result of generating standing wave at specific frequency. Recently, Chen *et al.* [34,35] proposed a wave-dominated energy transport mechanism in the study for graphene and boron nitride nanostructures, the mechanism is similar to that of the standing wave which dominates the vibration in graphene-carbon nanotube junctions at the narrow side in our work. To provide a concise physical picture for the standing wave, the temperature profile of GN-SWCNT(12, 12) with geometry size sets A along the heat transport direction is shown in fig. 5. It can be seen that the temperature profile behaves as periodic undulation due to the existence of the standing wave.

The resonance effect on thermal transport has attracted substantial attention recently. Research has shown that a metamaterials approach that relies on localized resonances holds great promise for engineering nanoscale heat transport [36–39]. Xiong *et al.* [36] found that combining designed resonant structures to alloying can lead to extremely low thermal conductivity in silicon nanowires. Davis *et al.* [38] investigated the local resonance results of reducing thermal conductivity in periodic arrays of pillars erected on free surfaces. Recently, the standing wave induced by local resonance is found and suggested as another important mechanism for TR in graded nanostructures [16,17]. The standing waves generally occur at the region near the narrow end of the graded nanostructure when the narrow end is at a higher temperature than the wide end. The existence of the standing wave greatly hinders the propagation of phonon waves as well as the transfer of thermal energy. In fact, thermal rectification in a nanostructure may be induced by more than one mechanism, such as asymmetric effect, phonon spectra overlap, inseparable dependence of thermal conductivity on temperature and space, the standing wave and phonon edge localization, and some of these mechanisms should be interrelated and inseparable. In this work, the ultrahigh TR ratio in GN-CNT junctions is attributed to the comprehensive effect by both size asymmetric boundary thermal contacts and the standing wave induced by local resonance, however analysis of the ration between these two rectifying mechanisms is rather difficult because these two mechanisms is interrelated.

In the present work, the unusually high TR from the GN-CNT junctions is attributable to the resonance effect on thermal transport. For the GN-CNT junction, the strong local resonance-induced standing wave appeared near the tube ends and greatly reduced thermal conductivity under negative temperature bias but not under positive temperature bias, resulting in preferential heat/phonon flow in one direction. For example, for the GN-SWCNT(12, 12) junction with geometric size set A, the thermal conductivity λ and thermal resistance R along the longitudinal direction of the tube are, respectively, $24.6\,\mathrm{Wm^{-1}K^{-1}}$ and $1.04\times10^{8}\,\mathrm{K/W}$ when $\Delta = 0.5$. When $\Delta = -0.5$, however, the thermal conductivity λ declines significantly to $1.55\,\mathrm{Wm^{-1}K^{-1}}$ and the thermal resistance R increases to $1.65\times10^{9}\,\mathrm{K/W}$. For the GN-SWCNT(6, 6) junction with maximum $\eta = 1244.1\%$ at a temperature of 300 K reported in previous work [24], λ and R are, respectively, $23.1\,\mathrm{Wm^{-1}K^{-1}}$ and $2.21\times10^{8}\,\mathrm{K/W}$ when $\Delta = 0.5$; however, λ declined to $1.72\,\mathrm{Wm^{-1}K^{-1}}$ and the R increased to $2.97\times10^{9}\,\mathrm{K/W}$ when $\Delta = -0.5$. The local resonance leads to a more heavily thermal conductivity reduction for the GN-SWCNT(12, 12) junction under negative thermal bias than that for the GN-SWCNT(6, 6) junction, thus making a higher TR ratio in the GN-SWCNT(12, 12) junction.

Conclusions. – In summary, thermal rectification from the GN-SWCNT(12, 12) junction is investigated via MD simulations. We find that the TR ratio of the GN-SWCNT junction can be tuned dramatically by controlling the chirality of the pillar. The thermal rectification ratio of the GN-SWCNT(12,12) junction can respectively reach up to 1487% and 2586.4% at temperatures of 300 K and 200 K ($|\Delta| = 0.5$), much higher than those previously reported for the graded PGS and GN-CNT junction by SWCNT(6, 6). The influences of the geometric parameters on the thermal rectification are discussed, and the underlying mechanism is explored. The results reveal that the local resonance and their induced standing wave are the underlying physical mechanism behind the ultrahigh thermal rectification. This study provides a guidance for application of the GN-CNT junction and their based PGS in thermal management.

* * *

The authors acknowledge the support provided by the National Natural Science Foundation of China (Grant No. 51576066).

REFERENCES

[1] Dimitrakakis G. K., Tylianakis E. and Froudakis G. E., *Nano Lett.*, **8** (2008) 3166.
[2] Du F., Yu D., Dai L., Ganguli S., Varshney V. and Roy A. K., *Chem. Mater.*, **23** (2011) 4810.

[3] Lakshmanan A., Srivastava S., Ramazani A. and Sundararaghavan V., *Appl. Phys. Lett.*, **112** (2018) 151902.

[4] Chen J., Walther J. H. and Koumoutsakos P., *Adv. Funct. Mater.*, **25** (2015) 7539.

[5] Lin J., Zhong J., Bao D., Reiber-kyle J. and Wang W., *J. Nanosci. Nanotechnol.*, **12** (2012) 1770.

[6] González J., Guinea F. and Herrero J., *Phys. Rev. B*, **79** (2009) 165434.

[7] González J. and Herrero J., *Nucl. Phys. B*, **825** (2010) 426.

[8] Sakhavand N. and Shahsavari R., *ACS Appl. Mater. Interfaces*, **9** (2017) 39122.

[9] Shi J., Dong Y., Fisher T. and Ruan X., *J. Appl. Phys.*, **118** (2015) 044302.

[10] Park J. and Prakash V., *J. Mater. Res.*, **28** (2013) 940.

[11] Xu L., Wei N., Zheng Y., Fan Z., Wang H. Q. and Zheng J. C., *J. Mater. Chem.*, **22** (2012) 1435.

[12] Zhang Z., Kutana A., Roy A. and Yakobson B. I., *J. Phys. Chem. C*, **121** (2017) 1257.

[13] Ye Z. Q. and Cao B. Y., *Nanoscale*, **9** (2017) 11480.

[14] Zhang T. and Luo T., *Small*, **11** (2015) 4657.

[15] Wang Y., Vallabhaneni A., Hu J., Qiu B., Chen Y. P. and Ruan X., *Nano Lett.*, **14** (2014) 592.

[16] Liu Y. Y., Zhou W. X. and Chen K. Q., *Sci. Rep.*, **5** (2015) 17525.

[17] Liu Y. Y., Zhou W. X., Tang L. M. and Chen K. Q., *Appl. Phys. Lett.*, **105** (2014) 203111.

[18] Hu S., An M., Yang N. and Li B., *Small*, **13** (2017) 1602716.

[19] Chen S., Pereira E. and Casati G., *EPL*, **111** (2015) 30004.

[20] Pons M., Cui Y. Y., Ruschhaupt A., Simón M. A. and Muga J. G., *EPL*, **119** (2017) 64001.

[21] Zhang L., Thingna J., He D., Wang J. S. and Li B., *EPL*, **103** (2013) 64002.

[22] Sun T., Wang J. and Kang W., *EPL*, **105** (2014) 16004.

[23] Yang X., Yu D., Cao B. and To A. C., *ACS Appl. Mater. Interfaces*, **9** (2017) 29.

[24] Yang X., Yu D. and Cao B., *ACS Appl. Mater. Interfaces*, **9** (2017) 24078.

[25] Plimpton S., *J. Comput. Phys.*, **117** (1995) 1.

[26] Lindsay L. and Broido D. A., *Phys. Rev. B*, **81** (2010) 205441.

[27] Berendsen H. J., Postma J. V., Van Gunsteren W. F., Dinola H. J. and Haak J. R., *J. Chem. Phys.*, **81** (1984) 3684.

[28] Ai B. Q. and Hu B., *Phys. Rev. E*, **83** (2011) 011131.

[29] Wu G. and Li B., *J. Phys.: Condens. Matter*, **20** (2008) 175211.

[30] Ouyang T., Chen Y., Xie Y., Wei X. L., Yang K., Yang P. and Zhong J., *Phys. Rev. B*, **82** (2010) 245403.

[31] Cao H. Y., Xiang H. and Gong X. G., *Solid State Commun.*, **152** (2012) 1807.

[32] Zhong W. R., Huang W. H., Deng X. R. and Ai B. Q., *Appl. Phys. Lett.*, **99** (2011) 193104.

[33] Chen X. K., Xie Z. X., Zhou W. X., Tang L. M. and Chen K. Q., *Carbon*, **100** (2016) 492.

[34] Chen X. K., Xie Z. X., Zhou W. X., Tang L. M. and Chen K. Q., *Appl. Phys. Lett.*, **109** (2016) 023101.

[35] Chen X. K., Liu J., Peng Z. H., Du D. and Chen K. Q., *Appl. Phys. Lett.*, **110** (2017) 091907.

[36] Xiong S., Sääskilahti K., Kosevich Y. A., Han H., Donadio D. and Volz S., *Phys. Rev. Lett.*, **117** (2016) 025503.

[37] Chen J., Zhang G. and Li B., *J. Chem. Phys.*, **135** (2011) 104508.

[38] Davis B. L. and Hussein M. I., *Phys. Rev. Lett.*, **112** (2014) 055505.

[39] Honarvar H. and Hussein M. I., *Phys. Rev. B*, **93** (2016) 081412.